

radiation. On the one hand, as noted above, the increased photoevaporation of the disk surface might load material onto magnetic field lines, which should produce a heavier jet. On the other hand, the role that strong radiation fields have on the region of jet collimation is unstudied, and it is conceivable that formation of a normal jet might be impeded on the illuminated side. Although the well developed jet is also exposed, the point of launch and collimation may lie in the shadow of a small circumstellar disk that remains undetected in our data and is thus only illuminated by the diffuse ultraviolet field. The best-developed jet, HH444, shows a normal shock-excited [S II] bright region at the base of the jet, which rapidly changes to an H α dominated seemingly photoionized spectrum further away from the driving source.

If these jets are photoionized, this opens the possibility of determining fundamental jet parameters like the mass-loss rate much more accurately than is possible for common shock-excited jets. A jet with a steady, constant mass loss rate and a sound speed c_s will widen at an angle given by $2c_s/v_j$ where v_j is the jet velocity. Therefore, the jet density declines as r^{-2} , where r is the distance from the jet source. As the jet emerges from the shadow of the small disk associated with its source star, ultraviolet radiation will rapidly ionize the skin of the jet until the total recombination rate in the photoionized zone just balances the incident ionizing flux. In this region the jet contains both a neutral core and a photoionized exterior. However, the divergence of the jet ensures that it eventually becomes fully ionized as it moves beyond a distance given by $r_{\max} = 4.6 \times 10^{16} \sin^{-1/3}(\theta) \dot{M}_{-8}^{2/3} V_{200}^{1/3} c_{10}^{-1} Q_{48}^{-1/3} d_3^{-1}$ cm, where \dot{M}_{-8} is the jet mass-loss rate in units of 10^{-8} solar masses per year, V_{200} is the jet velocity in units of 200 km s^{-1} , c_{10} is the sound speed in units of 10 km s^{-1} , Q_{48} is the number of ionizing photons emitted by σ Orionis in units of 10^{48} photons s^{-1} , d_3 is the distance between σ Orionis and the jet in units of 3 pc, and θ is the angle between the jet axis and the arrival direction of the ionizing photons. (We assume that the jet density at any particular distance from its source star is uniform across the jet, and we ignore the diffuse radiation field). An irradiated jet with the above parameters set to unity is expected to become fully ionized when the density drops below about 600 cm^{-3} , which is the jet density at $r_{\max} = 4.6 \times 10^{16} \text{ cm}$ (equivalent to $7''$ to $9''$ at 360 to 470 pc). This is in good agreement with observations of HH444, where [O I] emission tracing neutral material extends for about $8''$ to $10''$ from V510 Orionis (knots B and C). The [S II] line ratio in knots B and C indicates an electron density n_e of about $330 \pm 30 \text{ cm}^{-3}$. If the jet becomes fully ionized beyond this point, then this density should agree with that which can be derived from the H α surface brightness (proportional to the emission measure $n_e^2 l$ where l is the thickness of the jet); this implies that the jet is about 450 AU in diameter (about $1''$) and transports mass at a rate of about $5 \times 10^{-8}/V_{200}$ solar masses per year through knots B and C. More detailed future observations of irradiated jets could be used to measure directly the density and mass in a jet as a function of distance from its source, leading to better determinations of mass loss rates from young stars. \square

Received 30 April; accepted 4 September 1998.

- Shu, F. H., Najita, J., Wilkin, F., Ruden, S. P. & Lizano, S. Magnetocentrifugally driven flows from young stars and disks. I. A generalized model. *Astrophys. J.* **429**, 781–796 (1994).
- Ouyed, R., Pudritz, R. E. & Stone, J. Episodic jets from black holes and protostars. *Nature* **385**, 409–414 (1997).
- Johnstone, D., Hollenbach, D. & Bally, J. Photoevaporation of disks and clumps by nearby massive stars: application to disk destruction in the Orion Nebula. *Astrophys. J.* **499**, 758–776 (1998).
- Hoffleit, D. *The Bright Star Catalogue* (Yale Univ., New Haven, CT, 1982).
- Brown, A. G. A. *Stellar Content and Evolution of OB Associations*. Thesis, Univ. Leiden (1996).
- Warren, W. H. & Hesser, J. E. A photometric study of the Orion OB1 association. III-Subgroup analyses. *Astrophys. J. Supp.* **36**, 497–572 (1978).
- Blaauw, A. in *The Physics of Star Formation and Early Stellar Evolution* (eds Lada, C. J. & Kylafis, N. D.) 125–154 (NATO ASI Ser. C, Vol. 342, Kluwer, Dordrecht, 1991).
- de Zeeuw, P. T., Hoogerwerf, R., de Bruijne, J. H. J., Brown, A. G. A. & Blaauw, A. A Hipparcos census of the nearby OB associations. *Astron. J.* (in the press).
- Wiramihardja, S. D., Kogure, T., Yoshida, S., Ogura, K. & Nakano, M. Survey observations of emission-line stars in the Orion region. I. The Kiso area A-0904. *Publ. Astron. Soc. Jpn* **41**, 155–174 (1989).
- Wolk, S. J. *Watching the Stars Go 'Round and 'Round*. Thesis, State Univ. New York at Stony Brook (1996).

- Walter, F. M., Wolk, S. J. & Sherry, W. The Sigma Orionis Cluster. In *Cool Stars, Stellar Systems, and the Sun 10* (eds Donahue, R. & Bookbinder, J.) (ASP Conf. Ser., in the press).
- Reipurth, B. & Heathcote, S. in *Herbig-Haro Flows and the Birth of Low Mass Stars* (eds Reipurth, B. & Bertout, C.) 3–18 (IAU Symp. 182, Kluwer, Dordrecht, 1997).
- Hartmann, L. in *Herbig-Haro Flows and the Birth of Low Mass Stars* (eds Reipurth, B. & Bertout, C.) 391–404 (IAU Symp. 182, Kluwer, Dordrecht, 1997).
- Cernicharo, J., LeFloch, B., Garcia López, R. & Esteban, C. in *Low Mass Star Formation—from Infall to Outflow* (eds Malbet, F. & Castets, A.) 8–10 (Observ. de Grenoble, 1997).
- Sanduleak, N. Detection of T Tauri-like spectra in six stars in Orion. *Publ. Astron. Soc. Pacif.* **83**, 95–97 (1971).
- Mundt, R. & Bastian, U. UVB photometry of young emission-line objects. *Astron. Astrophys. Suppl.* **39**, 245–250 (1980).
- Herbig, G. H. & Bell, K. R. Third catalog of emission-line stars of the Orion population. *Lick Observ. Bull.* No. 1111 (1988).
- Graham, J. A. Objects associated with low-mass star formation in the Gum Nebula. *Astrophys. J.* **302**, 352–362 (1986).
- Hirth, G. A., Mundt, R. & Solf, J. Spatial and kinematic properties of the forbidden emission line region of T Tauri stars. *Astron. Astrophys. Suppl.* **126**, 437–469 (1997).
- Solf, J. in *ESO Workshop on Low Mass Star Formation and Pre-Main Sequence Objects* (ed. Reipurth, B.) 399–406 (ESO, Garching, 1989).
- Gorti, U. & Bhatt, H. C. Orbital decay of protostellar binaries in molecular clouds. *Mon. Not. R. Astron. Soc.* **283**, 566–576 (1996).
- Clarke, C. J. & Syer, D. Low-mass companions to T Tauri stars: a mechanism for rapid-rise FU Orionis outbursts. *Mon. Not. R. Astron. Soc.* **278**, L23–L27 (1996).
- Herbig, G. H. The young cluster IC 348. *Astrophys. J.* **497**, 736–758 (1998).
- Reipurth, B., Bally, J., Graham, J. A., Lane, A. P. & Zealey, W. The jet and energy source of HH 34. *Astron. Astrophys.* **164**, 51–66 (1986).
- Reipurth, B. & Heathcote, S. The jet and energy source of HH 46/47. *Astron. Astrophys.* **246**, 511–534 (1991).
- Reipurth, B. The HH 111 jet and multiple outflow episodes from young stars. *Nature* **340**, 42–45 (1989).
- Gredel, R. & Reipurth, B. An infrared counter-flow in the HH 111 jet complex. *Astron. Astrophys.* **289**, L19–L22 (1994).
- Zinnecker, H., McCaughrean, M. J. & Rayner, J. T. A symmetrically pulsed jet of gas from an invisible protostar in Orion. *Nature* **394**, 862–865 (1998).
- Hirth, G. A., Mundt, R., Solf, J. & Ray, T. P. Asymmetries in bipolar jets from young stars. *Astrophys. J.* **427**, L99–L102 (1994).

Acknowledgements. We thank A. Raga and D. Hollenbach for discussions, L.-Å. Nyman for a CO measurement, D. Theil for help in producing the figures, and M. McCaughrean and R. Ouyed for comments and advice.

Correspondence and requests for materials should be addressed to B.R. (e-mail address: reipurth@casa.colorado.edu).

Spin domains in ground-state Bose-Einstein condensates

J. Stenger, S. Inouye, D. M. Stamper-Kurn, H.-J. Miesner, A. P. Chikkatur & W. Ketterle

Department of Physics and Research Laboratory of Electronics, Massachusetts Institute of Technology, Cambridge, Massachusetts 02139, USA

Bose-Einstein condensates—a low-temperature form of matter in which a macroscopic population of bosons occupies the quantum-mechanical ground state—have been demonstrated for weakly interacting, dilute gases of alkali-metal^{1–3} and hydrogen²⁵ atoms. Magnetic traps are usually employed to confine the condensates, but have the drawback that spin flips in the atoms lead to untrapped states. For this reason, the spin orientation of the trapped alkali atoms cannot be regarded as a degree of freedom. Such condensates are therefore described by a scalar order parameter, like the spinless superfluid ⁴He. In contrast, a recently realized optical trap⁴ for sodium condensates confines atoms independently of their spin orientations. This offers the possibility of studying ‘spinor’ condensates in which spin comprises a degree of freedom, so that the order parameter is a vector rather than scalar quantity. Here we report the observation of equilibrium states of sodium spinor condensates in an optical trap. The freedom of spin orientation leads to the formation of spin domains in an external magnetic field, which can be either miscible or immiscible with one another.

A variety of new phenomena are predicted^{5–7} for spinor condensates, such as spin textures, propagation of spin waves and coupling between superfluid flow and atomic spin. To date, such effects could only be studied in superfluid ³He, which can be

described by Bose–Einstein condensation of Cooper pairs of quasi-particles having both spin and orbital angular momentum⁸. Compared to the strongly interacting ³He, the properties of weakly interacting Bose–Einstein condensates of alkali-metal gases can be calculated by mean field theories in a much more straightforward and simple way.

Other systems which go beyond the description with a single scalar order parameter are condensates of two different hyperfine states of ⁸⁷Rb confined in magnetic traps. Recent experimental studies have explored the spatial separation of the two components^{9,10} and their relative phase¹¹. Several theoretical papers describe their structure^{12–18} and their collective excitations^{19–22}.

Compared to these two-component condensates, spinor condensates have several new features, including the vector character of the order parameter and the changed role of spin relaxation collisions which allow for population exchange among hyperfine states without trap loss. In contrast, for ⁸⁷Rb experiments trap loss due to spin relaxation severely limits the lifetime.

Here we consider an $F = 1$ spinor condensate subject to spin relaxation, in which two $m_F = 0$ atoms can collide and produce an $m_F = +1$ and an $m_F = -1$ atom and vice versa. (Here, F denotes the angular momentum per atom and m_F its magnetic quantum number.) We investigate the distribution of hyperfine states and the spatial distribution in equilibrium assuming conservation of the total spin.

The ground state spinor wavefunction is found by minimizing the free energy⁵;

$$K = \int d^3r n \left[V + \frac{c_0 n}{2} + \frac{c_2 n}{2} \langle \mathbf{F} \rangle^2 + E_{ze} - p_0 \langle F_z \rangle \right] \quad (1)$$

where kinetic energy terms are neglected in the Thomas–Fermi approximation which is valid as long as the dimension of spin domains (typically 50 μm) is larger than the penetration depth¹⁸ (typically 1 μm). V is trapping potential, n is the density, r is the spatial coordinate and E_{ze} is the Zeeman energy in an external magnetic field. The Lagrange multiplier p_0 accounts for the total spin conservation. The mean field energy in equation (1) consists of a spin-independent part proportional to c_0 and a spin-dependent part proportional to $c_2 \langle \mathbf{F} \rangle^2$. The coefficients c_0 and c_2 are related to the scattering lengths a_0 and a_2 for two colliding atoms with total angular momentum $F_{\text{tot}} = 0$ or $F_{\text{tot}} = 2$ by $c_0 = 4\pi\hbar^2 \bar{a}/M$ and $c_2 = 4\pi\hbar^2 \Delta a/M$ with $\bar{a} = (2a_2 + a_0)/3$, $\Delta a = (a_2 - a_0)/3$, and M for the atomic mass (ref. 5). The spin-dependent interaction originates from the term $c_2 \mathbf{F}_1 \cdot \mathbf{F}_2$ in the interaction of two atoms, which is ferromagnetic for $c_2 < 0$ and antiferromagnetic for $c_2 > 0$.

In the Bogoliubov approach, the many-body ground-state wavefunction is represented by the spinor wavefunction;

$$\Psi(\mathbf{r}) = \sqrt{n(\mathbf{r})} \zeta(\mathbf{r}) = \sqrt{n(\mathbf{r})} (\zeta_+(\mathbf{r}), \zeta_0(\mathbf{r}), \zeta_-(\mathbf{r})) \quad (2)$$

where ζ_+ , ζ_0 , ζ_- denote the amplitudes for the $m_F = +1, 0, -1$ states, respectively, and $|\zeta|^2 = 1$.

The Zeeman energy E_{ze} is given by;

$$E_{ze} = E_+ |\zeta_+|^2 + E_0 |\zeta_0|^2 + E_- |\zeta_-|^2 = E_0 - \bar{p} \langle F_z \rangle + q \langle F_z^2 \rangle \quad (3)$$

where E_+ , E_0 , E_- are the Zeeman energies of the $m_F = +1, 0, -1$ states, $2q \equiv E_+ + E_- - 2E_0$ is the Zeeman energy difference in a spinflip collision, and $2\bar{p} \equiv E_- - E_+$. The E_0 term can be included in the trapping potential V . The parameter \bar{p} can be combined with the Lagrange multiplier p_0 to give $p \equiv \bar{p} + p_0$.

In the following we determine the spinor which minimizes the spin-dependent part K_s of the free energy:

$$K_s = c \langle \mathbf{F} \rangle^2 - p \langle F_z \rangle + q \langle F_z^2 \rangle \quad (4)$$

where $c = c_2 n/2$. The minimization of equation (4) for different values of the parameters c , p and q is straightforward, and is shown

graphically in the form of spin-domain diagrams in Fig. 1.

Experimentally, the values of c , p and q can be varied arbitrarily, representing any region of the spin-domain diagram. The magnitude (but not the sign) of the coefficient c is varied by changing the density n , either by changing the trapping potential, or by studying condensates with different numbers of atoms. In this study, the axial length of the trapped condensate is more than 60 times larger than its radial size, and thus we consider the system one-dimensional, and integrate over the radial coordinates, obtaining $n = 2n_0/3$ where n_0 is the density at the radial centre. This integration assumes a parabolic density profile within the Thomas–Fermi approximation. The value of q can be changed by applying a weak external bias field B_0 : q then corresponds to the quadratic Zeeman shift which is proportional to B_0^2 . The coefficient p arises both from the linear Zeeman shift and from the Lagrange multiplier p_0 which is determined by the total spin of the system. For a system with zero total spin in a homogenous bias field B_0 , p_0 cancels the linear Zeeman shift due to B_0 , yielding $p = 0$. Positive (negative) values of p are achieved for condensates with a positive (negative) overall spin. Finally, the coefficients can be made to vary spatially across the condensate. In particular, applying a field gradient B' along the axis of the trapped condensate causes p to vary along the condensate length. For a condensate with zero total spin, p is proportional to $B'z$ where z is the axial coordinate with $z = 0$ at the centre of the condensate. Thus, the condensate samples a vertical line in the spin-domain diagrams of Fig. 1. The centre of this line lies at $p = 0$, and its length is given by the condensate length scaled by B' .

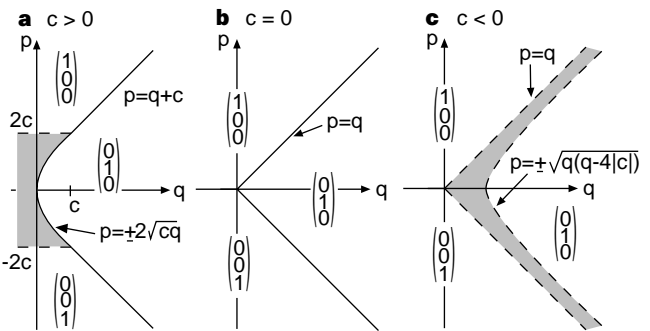


Figure 1 Spin-domain diagrams for condensates with $F = 1$. The structure of the ground-state spinor is shown as a function of the linear ($\sim p$) and quadratic ($\sim q$) Zeeman energies. Hyperfine components are mixed inside the shaded regions. Solid lines indicate a discontinuous change of state populations whereas dashed lines indicate a gradual change. The behaviour for $q < 0$ is also shown, although it is not relevant for the experiment reported here. For $c = 0$, the Zeeman energy causes the cloud to separate into three domains with $m_F = +1, 0, -1$ and with boundaries at $|p| = q$, as shown in **b**. For $c \neq 0$, the mean field energy shifts the boundary region between domains and leads to regions of overlapping spin components. In the antiferromagnetic case (**a**), the $m_F = 0$ component and the $m_F = \pm 1$ components are immiscible (including the kinetic energy terms in equation (1) would lead to a thin boundary layer) and the boundary occurs at $|p| = q + c$. For small bias fields, with $q < c$ and $|p| < 2c$, the $m_F = 0$ domain is bordered by domains in which $m_F = \pm 1$ components are mixed. The ratio of the $m_F = \pm 1$ populations in these regions does not depend on q , but is given by $|\zeta_+|^2/|\zeta_-|^2 = (2c + p)/(2c - p)$. In this region of small fields, the boundary to the $m_F = 0$ component lies at $|p| = 2\sqrt{cq}$. In the ferromagnetic case (**c**) all three components are generally miscible, and have no sharp boundaries. Pure $m_F = 0$ domains occur for $|p| \leq \sqrt{q(q - 4|c|)}$ and pure $m_F = \pm 1$ domains for $|p| > q$. Here, in contrast to the antiferromagnetic case, a pure $m_F = 0$ condensate is skirted by regions where it is mixed predominantly with either the $m_F = -1$ or the $m_F = +1$ component. The contribution of the third component is very small ($< 2\%$). In all mixed regions, the $m_F = 0$ component is never the least populated of the three spin components. This qualitative feature can be used to rule out the possibility that $F = 1$ sodium atoms have ferromagnetic interactions.

Our experimental study of spinor condensates required techniques to selectively prepare and probe condensates in arbitrary hyperfine states. Spinor condensates were prepared in several steps. Laser cooling and evaporative cooling were used to produce sodium condensates in the $m_F = -1$ state in a cloverleaf magnetic trap²³. The condensates were then transferred into an optical dipole trap consisting of a single focused infrared laser beam⁴. After the spin preparation, a bias field B_0 and a field gradient B' were applied for a variable amount of time (as long as 30 s), during which the atoms relaxed towards their equilibrium distribution (Fig. 2).

The profiles in Fig. 3 were obtained from vertical cuts through absorption images. They provide clear evidence of antiferromagnetic interaction. (The opposite case is predicted for the $^{87}\text{Rb } F = 1$ spin multiplet²⁴.) The spin structure is consistent with the corresponding spin-domain diagram in Fig. 1a. Overlapping $m_F = \pm 1$ clouds as observed are incompatible with the assumption of ferromagnetic interaction.

The strength $c = (50 \pm 20)$ Hz of the antiferromagnetic interaction was estimated by determining z_b , the location of the $m_F = 0$ to the $m_F = \pm 1$ boundary, and by plotting $p = \mu B' z_b$ versus the quadratic Zeeman shift $q = \hat{q} B_0^2$ (Fig. 4). The constants μ and \hat{q} are defined in the figure legend. With $n = (2.9 \pm 0.5) \times 10^{14} \text{ cm}^{-3}$, the difference between the scattering

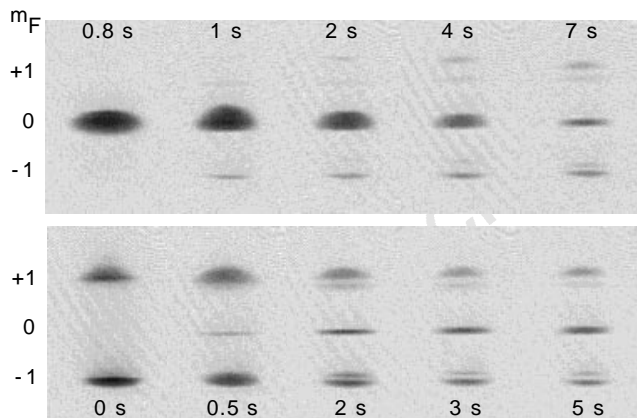


Figure 2 Formation of ground-state spin domains. Absorption images of ballistically expanding spinor condensates show both the spatial and hyperfine distributions. Arbitrary populations of the three hyperfine states were prepared using r.f. transitions (Landau-Zener sweeps)⁴. At a bias field of ~ 40 G, the transitions from $m_F = -1$ to $m_F = 0$ and from $m_F = 0$ to $m_F = +1$ differ in frequency by ~ 0.9 MHz due to the quadratic Zeeman shift, and they could be driven separately. The images of clouds with various dwell times in the trap show the evolution to the same equilibrium for condensates prepared in either a pure $m_F = 0$ state (upper row) or in equally populated $m_F = \pm 1$ states (lower row). Between 5 and 15 s dwell time, the distribution did not change significantly, although the density decreased due to three-body recombination. The bias field during the dwell time was $B_0 = 20$ mG, and the field gradient was $B' = 11 \text{ mG cm}^{-1}$. These images were taken after the optical trap was suddenly switched off, and the atoms were allowed to expand. Due to the large aspect ratio (typically 60), the expansion was almost purely in the radial directions. All the mean-field energy was released after < 1 ms, after which the atoms expanded as free particles. Thus, a magnetic field gradient, which was applied after 5 ms time of flight to yield a Stern-Gerlach separation of the cloud, merely translated the three spin components without affecting their shapes. In this manner, the single time-of-flight images provided both a spatial and spin-state description of the trapped cloud. Indeed, the shapes of the three clouds fit together to form a smooth total density distribution. After a total time of flight of 25 ms, the atoms were optically pumped into the $F = 2$ hyperfine state and observed using the $m_F = +2$ to $m_F = +3$ cycling transition. This technique assured the same transition strength for atoms originating from different spin states. The size of the field of view for a single spinor condensate is 1.7×2.7 mm.

lengths can be determined to $a_2 - a_0 = 3\Delta a = (3.5 \pm 1.5)a_B = (0.19 \pm 0.08) \text{ nm}$ where a_B is the Bohr radius. This result is in rough agreement with a theoretical calculation of $a_2 - a_0 = (5.5 \pm 0.5)a_B$ (ref. 24). The antiferromagnetic interaction energy corresponds to 2.5 nK in our condensates. Still, the magnetostatic (ferromagnetic) interaction between the atomic magnetic moments is about ten times weaker. We note that the optically trapped samples in which the domains were observed were at a temperature of the order of 100 nK, far larger than the antiferromagnetic energy. The formation of spin domains occurs only in a Bose-Einstein condensate.

Figure 3c shows a profile of the density distribution for a cloud at $B_0 = 20$ mG and almost-cancelled gradient ($B' < 2 \text{ mG cm}^{-1}$). No $m_F = 0$ region can be identified. The cloud was prepared with a small total angular momentum. Due to the almost-zero gradient and the non-zero angular momentum, the cloud corresponds to a point in the shaded region in Fig. 1a, rather than a vertical line with no offset as discussed before with finite gradients and zero angular momentum. The different widths of the profiles are probably caused by residual field inhomogeneities. Figure 3c demonstrates the complete miscibility of the $m_F = \pm 1$ components.

For a homogenous two-component system the criterion for miscibility (immiscibility) is^{14,15,18} $a_{ab} < (>) \sqrt{a_a a_b}$, when the mean

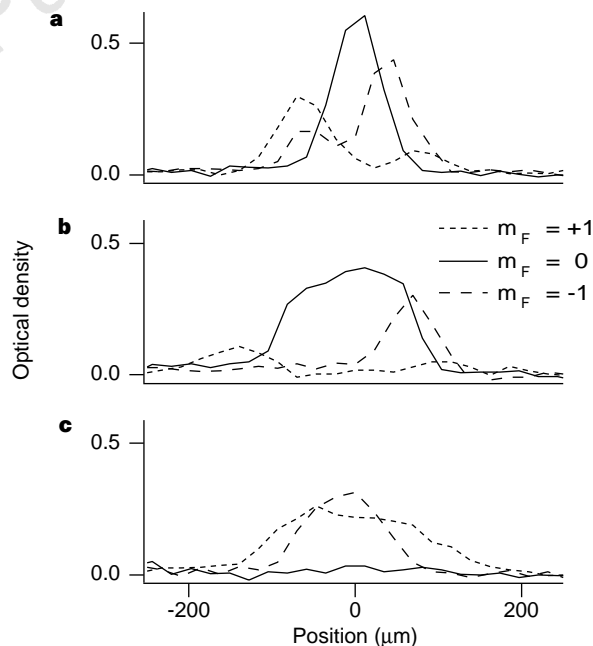


Figure 3 Miscible and immiscible spin domains. Axial column density profiles of spinor Bose-Einstein condensates are shown, obtained from time-of-flight absorption images as in Fig. 2. The profiles of the $m_F = \pm 1$ components were shifted to undo the Stern-Gerlach separation. At low bias fields (**a**), the $m_F = 0$ component was skirted on both sides by $m_F = \pm 1$ components with significant $m_F = \mp 1$ admixtures, thus demonstrating the antiferromagnetic interaction (also visible in Fig. 2). At higher fields (**b**), the $m_F = \pm 1$ components are pushed apart further by a larger $m_F = 0$ component, and the $m_F = \mp 1$ admixtures vanish. They could not be resolved for quadratic Zeeman energies $q > 20$ Hz. The antiferromagnetic interaction leads to immiscibility of the $m_F = 0$ and the $m_F = \pm 1$ components. The kinetic energy in this boundary region, which is small compared to the total mean-field energy, is released in the axial direction. Due to this axial expansion of the cloud in the time of flight, and due to imperfections in the imaging system including the limited pixel resolution, the $m_F = 0$ to $m_F = \pm 1$ boundary is not sharp. Panel **c** demonstrates the complete miscibility of the $m_F = \pm 1$ components. The magnetic field parameters were $B_0 = 20$ mG, $B' = 11 \text{ mG cm}^{-1}$ in **a**, $B_0 = 100$ mG, $B' = 11 \text{ mG cm}^{-1}$ in **b**, and $B_0 = 20$ mG, $B' < 2 \text{ mG cm}^{-1}$ in **c**.

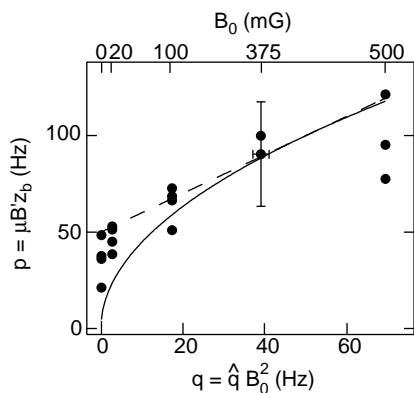


Figure 4 Estimate of the antiferromagnetic interaction energy c . Plotted is the linear Zeeman energy $p = |\mu_B z_b|$ at the boundary between the $m_F = 0$ and $m_F = \pm 1$ regions versus the quadratic Zeeman shift $q = \hat{q} B_0^2$. Here $\hat{q} = g_s^2 \mu_B^2 / 16 \hbar^2 \nu_{\text{hfs}} = 278 \text{ Hz G}^{-2}$, and $\mu = g_s \mu_B / 4 \hbar = 700 \text{ kHz G}^{-1}$, g_s denotes the electron g -factor, ν_{hfs} the hyperfine splitting frequency, and μ_B the Bohr magneton. The solid line is a fit of the function $|p| = 2\sqrt{qc}$ for $q < c$ and $|p| = q + c$ for $q > c$. Extrapolating the linear part to zero bias field (dashed line) yields $c = (50 \pm 20) \text{ Hz}$. The data points at a given bias field represent $p = \mu_B z_b$ for different gradient fields B' and thus $m_F = 0$ regions of different size. The scatter of these points is mainly due to residual magnetic field inhomogeneities, resulting in small deviations of the local gradient B' . The error bar represents the relative error of all data points of 30% in p and 5% in q , as estimated from the uncertainties in the magnetic-field calibration. Furthermore, the limited pixel resolution and contributions of the kinetic energy in the condensate to the axial expansion enhance the errors for the determination of z_b of small $m_F = 0$ regions.

field energy is parametrized as $(2\pi\hbar^2/M)(n_a^2 a_a + n_b^2 a_b + 2n_a n_b a_{ab})$. Here, $n_{a,b}$ and $a_{a,b}$ are densities and scattering lengths for the components a and b , and the scattering length a_{ab} characterizes the interactions between particles a and b . In our spinor condensate with mixtures of the $m_F = \pm 1$ components, we have $a_{-1} = a_{+1} = \bar{a} + \Delta a$ and $a_{-1+1} = \bar{a} - \Delta a$. Thus $\Delta a > 0$, as experimentally observed, implies miscibility. For a mixture of the $m_F = 1$ and $m_F = 0$ components, we find $a_0 = \bar{a}$, $a_{+1} = \bar{a} + \Delta a$ and $a_{0+1} = \bar{a} + \Delta a$, corresponding to immiscibility. For the ^{87}Rb experiments^{9,10}, it is not clear whether the two components are miscible or overlap only in a surface region due to kinetic energy (E. A. Cornell, personal communication).

All regions in the spin-domain diagrams are accessible with our experimental technique, and thus any combination of the three hyperfine components can be realized by applying small external magnetic fields. Of special interest for future work is the zero-magnetic-field case, where the rotational symmetry should be spontaneously broken. We observed both miscibility and immiscibility of hyperfine components. Thus the dynamics and possible metastable configurations⁷ of two interpenetrating, miscible superfluid components ($m_F = \pm 1$) with arbitrary admixtures of an immiscible component ($m_F = 0$) can now be studied. □

Received 18 June; accepted 3 September 1998.

1. Anderson, M. H., Ensher, J. R., Matthews, M. R., Wieman, C. E. & Cornell, E. A. Observation of Bose-Einstein condensation in a dilute atomic vapor. *Science* **269**, 198–201 (1995).
2. Davis, K. B. *et al.* Bose-Einstein condensation in a gas of sodium atoms. *Phys. Rev. Lett.* **75**, 3969–3973 (1995).
3. Bradley, C. C., Sackett, C. A. & Hulet, R. G. Bose-Einstein condensation of lithium: Observation of limited condensate number. *Phys. Rev. Lett.* **78**, 985–989 (1997).
4. Stamper-Kurn, D. M. *et al.* Optical confinement of a Bose-Einstein condensate. *Phys. Rev. Lett.* **80**, 2027–2030 (1998).
5. Ho, T.-L. Spinor Bose condensates in optical traps. *Phys. Rev. Lett.* **81**, 742–745 (1998).
6. Ohmi, T. & Machida, K. Bose-Einstein condensation with internal degrees of freedom in alkali atom gases. *J. Phys. Soc. Jpn* **67**, 1822–1825 (1998).
7. Law, C. K., Pu, H. & Bigelow, N. P. Quantum spins mixing in spinor Bose-Einstein condensates. *Phys. Rev. Lett.* (submitted); preprint cond-mat/9807258 at (<http://xxx.lanl.gov>) (1998).
8. Vollhardt, D. & Wölfle, P. *The Superfluid Phases of He* (Taylor-Francis, London, 1990).
9. Myatt, C. J., Burt, E. A., Ghrist, R. W., Cornell, E. A. & Wieman, C. E. Production of two overlapping Bose-Einstein condensates by sympathetic cooling. *Phys. Rev. Lett.* **78**, 586–589 (1997).

10. Hall, D. S., Matthews, M. R., Ensher, J. R., Wieman, C. E. & Cornell, E. A. The dynamics of component separation in a binary mixture of Bose-Einstein condensates. *Phys. Rev. Lett.* **81**, 1539–1542 (1998).
11. Hall, D. S., Matthews, M. R., Wieman, C. E. & Cornell, E. A. Measurements of relative phase in binary mixtures of Bose-Einstein condensates. *Phys. Rev. Lett.* **81**, 1543–1546 (1998).
12. Siggia, E. D. & Ruckenstein, A. E. Bose condensation in spin-polarized atomic hydrogen. *Phys. Rev. Lett.* **44**, 1423–1426 (1980).
13. Ho, T.-L. & Shenoy, V. B. Binary mixtures of Bose condensates of alkali atoms. *Phys. Rev. Lett.* **77**, 3276–3279 (1996).
14. Timmermans, E. Phase separation in Bose-Einstein condensates. *Phys. Rev. Lett.* (submitted); preprint cond-mat/9709301 at (<http://xxx.lanl.gov>) (1997).
15. Esry, B. D., Greene, C. H., Bruke, J. P. & Bohn, J. L. Hartree-Fock theory for double condensates. *Phys. Rev. Lett.* **78**, 3594–3597 (1997).
16. Öhberg, P. & Stenholm, S. Hartree-Fock treatment of the two-component Bose-Einstein condensate. *Phys. Rev. A* **57**, 1272–1279 (1998).
17. Pu, H. & Bigelow, N. P. Properties of two-species Bose condensates. *Phys. Rev. Lett.* **80**, 1130–1133 (1998).
18. Ao, P. & Chui, S. T. Binary Bose-Einstein condensate mixtures in weakly and strongly segregated phases. *Phys. Rev. A* **58**(6) (in the press).
19. Busch, T., Cirac, J. I., Pérez-García, V. M. & Zoller, P. Stability and collective excitations of a two-component Bose-Einstein condensed gas: a moment approach. *Phys. Rev. A* **56**, 2978–2983 (1997).
20. Graham, R. & Walls, D. Collective excitations of trapped binary mixtures of Bose-Einstein condensed gases. *Phys. Rev. A* **57**, 484–487 (1998).
21. Pu, H. & Bigelow, N. P. Collective excitations, metastability, and nonlinear response of a trapped two-species Bose-Einstein condensate. *Phys. Rev. Lett.* **80**, 1134–1137 (1998).
22. Esry, B. D. & Greene, C. H. Low-lying excitations of double Bose-Einstein condensates. *Phys. Rev. A* **57**, 1265–1271 (1998).
23. Mewes, M.-O. *et al.* Bose-Einstein condensation in a tightly confining dc magnetic trap. *Phys. Rev. Lett.* **77**, 416–419 (1996).
24. Burke, J. P., Greene, C. H. & Bohn, J. L. Multichannel cold collisions: simple dependencies on energy and magnetic field. *Phys. Rev. Lett.* **81**, 3355–3358 (1998).
25. Fried, D. G. *et al.* Bose-Einstein condensation of atomic hydrogen. *Phys. Rev. Lett.* (in the press).

Acknowledgements. We acknowledge discussions with J. Ho and C. Greene. This work was supported by the Office of Naval Research, NSF, Joint Services Electronics Program (ARO), NASA, and the David and Lucile Packard Foundation. J.S. acknowledges support from the Alexander von Humboldt foundation, D.M.S.-K. from the JSEP Graduate Fellowship Program, and A.P.C. from the NSF.

Correspondence and requests for materials should be addressed to J.S. (e-mail: stenger@amo.mit.edu).

Observation of smectic and moving-Bragg-glass phases in flowing vortex lattices

F. Pardo*, F. de la Cruz*, P. L. Gammel†, E. Bucher† & D. J. Bishop†

* Centro Atómico Bariloche and Instituto Balseiro, Comisión Nacional de Energía Atómica, 8400 S. C. de Bariloche, R. N., Argentina

† Bell Laboratories, Lucent Technologies, Murray Hill, New Jersey 07974, USA

The defining characteristic of the superconducting state is its ability to carry electrical currents without loss. The process by which it does this has been extensively studied for decades but there are still many unresolved issues. In particular, the critical current, which is the maximum electrical current that a superconductor can carry without loss, remains a poorly understood concept at the microscopic level. In a type II superconductor, a flux-line lattice (FLL) forms if a magnetic field between H_{c1} and H_{c2} , the lower and upper critical fields, is applied: flowing electrical currents will exert a force on this FLL. If the FLL remains pinned, the current flows without loss of energy and the effective resistance remains zero. However, if the lattice moves in response to the current, energy is dissipated and the zero-resistance state is lost. Because of its relevance to the critical current, the types of structures that these moving lattices can form have attracted much recent theoretical attention^{1–4}. Here we report magnetic decoration studies of flowing vortex lattices which show evidence for a transition, as a function of increasing flux density, from a layered (or smectic) FLL² to a more well-ordered moving Bragg glass¹.

Previous work on this problem has uncovered a number of results on the structures that can be formed by flowing vortices. Early imaging studies⁵ using small-angle neutron scattering (SANS) confirmed less-direct evidence from transport studies⁶, and found that while pinned lattices are disordered, flowing lattices can be